

Stochastic ion and electron heating on drift instabilities at the bow shock

Krzysztof Stasiewicz,^{1,2}*

¹*Department of Physics and Astronomy, University of Zielona Góra, Poland*

²*Space Research Centre, Polish Academy of Sciences, Warsaw, Poland*

Accepted 2020 May 11. Received 2020 April 01; in original form 2020 March 05

ABSTRACT

The analysis of the wave content inside a perpendicular bow shock indicates that heating of ions is related to the Lower-Hybrid-Drift (LHD) instability, and heating of electrons to the Electron-Cyclotron-Drift (ECD) instability. Both processes represent stochastic acceleration caused by the electric field gradients on the electron gyroradius scales, produced by the two instabilities. Stochastic heating is a single particle mechanism where large gradients break adiabatic invariants and expose particles to direct acceleration by the DC- and wave-fields. The acceleration is controlled by function $\chi = m_i q_i^{-1} B^{-2} \text{div}(\mathbf{E})$, which represents a general diagnostic tool for processes of energy transfer between electromagnetic fields and particles, and the measure of the local charge non-neutrality. The identification was made with multipoint measurements obtained from the Magnetospheric Multiscale spacecraft (MMS). The source for the LHD instability is the diamagnetic drift of ions, and for the ECD instability the source is ExB drift of electrons. The conclusions are supported by laboratory diagnostics of the ECD instability in Hall ion thrusters.

Key words: acceleration of particles – shock waves – solar wind – turbulence – chaos

1 INTRODUCTION

Terrestrial bow shock represents a great opportunity for investigation of various mechanisms for heating and acceleration of particles in collisionless plasmas with important implications for astrophysics. Since its discovery by Ness et al. (1964) there has been great deal of research on this collisionless shock wave (Wu et al. 1984; Gary 1993; Balikhin & Gedalin 1994; Lembége et al. 2003; Lefebvre et al. 2007; Treumann 2009; Burgess et al. 2012; Mozer & Sundqvist 2013; Breneman et al. 2013; Wilson III et al. 2014; Cohen et al. 2019), however, there is still no consensus on how particles are accelerated, and what exactly are processes that heat bulk plasma.

The observational advances afforded by multipoint measurements in space like Cluster (Escoubet et al. 1997), THEMIS (Sibeck & Angelopoulos 2008), and MMS (Burch et al. 2016) opened new possibilities for space plasma physics. In this report we provide arguments supported by measurements from the MMS mission, that a single, non-resonant, frequency independent mechanism can mediate heating of both ions and electrons at the bow shock. This mechanism relies on gradients of the electric field that en-

sure breaking of the magnetic moment, allowing for efficient, stochastic heating of particles by the present electric fluctuations, and even by the DC field.

The energisation process is controlled by a dimensionless function defined as

$$\chi(t, \mathbf{r}) = \frac{m_i}{q_i B^2} \nabla \cdot \mathbf{E} \equiv \frac{N_c}{N} \frac{c^2}{V_{Ai}^2} \quad (1)$$

for particles with mass m_i , charge q_i in fields $\mathbf{B}(t, \mathbf{r})$ and $\mathbf{E}(t, \mathbf{r})$. N_c is the number density of excess charges, N number density, $V_{Ai}^2 = B^2 / (\mu_0 N m_i)$, c - speed of light. The equivalent formula is obtained with substitution $\nabla \cdot \mathbf{E} = N_c q_i / \epsilon_0$. Stochastic heating occurs when $|\chi| > 1$. It is a single particle mechanism where large electric field gradients (or space charges) destabilise individual particle motion, rendering the trajectories chaotic in the sense of a positive Lyapunov exponent for initially nearby states. This condition has been known from some time, but the importance of $\text{div}(\mathbf{E})$ has not been recognised, and the directional gradient $\partial_x E_x$, or $k_\perp \nabla \phi$ was used in previous analyses or simulations (Cole 1976; McChesney et al. 1987; Karney 1979; Balikhin et al. 1993; Mishin & Banaszekiewicz 1998; Stasiewicz et al. 2000; Stasiewicz 2007; Vranjes & Poedts 2010; Stasiewicz et al. 2013; Yoon & Bellan 2019).

The recent MMS mission comprises four spacecraft

* E-mail: krzy.stasiewicz@gmail.com

flying in formation with spacing ~ 20 km and provides high quality 3-axis measurements of the electric field (Lindqvist et al. 2016; Ergun et al. 2016; Torbert et al. 2016), which we shall use to demonstrate applicability of (1) to heating of plasma at the bow shock. We use magnetic field vectors measured by the Fluxgate Magnetometer (Russell et al. 2016), the Search-Coil Magnetometer (Le Contel et al. 2016), and the number density, velocity, and temperature of both ions and electrons from the Fast Plasma Investigation (Pollock et al. 2016).

2 OBSERVATIONS

We show in Fig. 1 the time-frequency spectrogram of χ for the bow shock encountered by MMS on 2017-12-12T03:33:30 at position (8.9, 11.8, 4.9) R_E GSE. The shock had alfvénic and sound Mach numbers $M_A=8$, and $M_S=5$, and was strictly perpendicular. The timeseries for χ was derived from 4-point measurements using a general method for computing gradients in space developed for Cluster (Harvey 1998). Frequencies lower than 1 Hz have been removed from the analysis to ensure that calibration offsets, or satellite spin effects (0.05 Hz, and multiples) would not affect computations.

The spectrum of χ is similar to the usual power spectrum of the electric field, but weighted with B^{-2} so it emphasises the heating region in the foot/ramp of the shock, instead of the peak, where the power of E maximises, but there is no heating. It is sensitive to local charges related to electrostatic fields generated in plasma by waves and instabilities. Ideally, it should show distribution of electric charges, and time-domain variations at long wavelengths should vanish by subtraction. However, the spacecraft separation of 10–20 km does not make it possible to compute correctly gradients on scales ~ 1 km, which exist in this region.

We also show over-plots of the ion perpendicular temperature, electron temperature, (both in eV), and the lower-hybrid frequency $f_{lh} = f_{pp}/(1 + f_{pe}^2/f_{ce}^2)^{-1/2}$, where f_{pp} , f_{pe} are proton, electron plasma frequencies, f_{ce} electron gyrofrequency. The f_{lh} , f_{ce} plots represent the density and magnetic field variations across the shock, which should help the reader to position the foot and the ramp of the shock. The proton gyrofrequency $f_{cp} = 0.1\text{--}0.4$ Hz, is just below the bottom line of the picture.

The power of χ correlates well with regions of ion and electron heating, which is not true for the power spectrum of the electric field. A well known fact is that heating of ions is not co-located with heating of electrons, as seen also in the picture. Evident in the picture is a turbulent cascade that appears to transfer energy from lower frequency modes at the bottom to higher frequencies in localised striations extending to 4096 Hz, the upper frequency of measurements. Waves above f_{lh} are identified further as LHD and above f_{ce} as ECD.

We now turn to a different technique of signal analysis – namely, multiresolution frequency decomposition using orthogonal wavelets (Mallat 1999). This technique differs from pass-band filtering. Orthogonal decomposition is exact; the signal is divided into discrete frequency dyads that form $2^{-n}f_N$ hierarchy starting from the Nyquist frequency f_N . Orthogonality means that time integral of any pair of

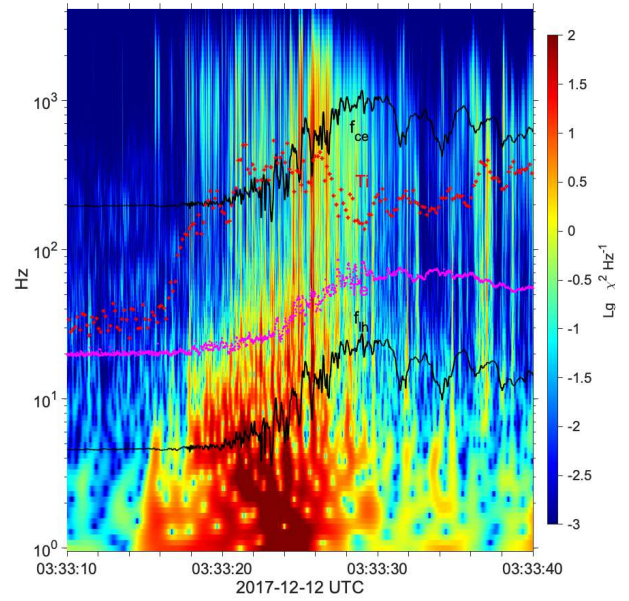


Figure 1. Power spectrum of χ across the perpendicular bow shock. Over-plotted are: the lower-hybrid frequency f_{lh} (black), temperatures, $T_{e\perp}$ (magenta), $T_{i\perp}$ (red), both in eV, and electron cyclotron frequency f_{ce} . At the bottom up to f_{lh} there are oblique whistler waves, followed by striations of Lower-Hybrid-Drift waves in the range $f_{lh} - f_{ce}$ that extend as Electron-Cyclotron-Drift waves above f_{ce} .

the frequency dyads is zero. The decomposed electric field is shown in Fig. 2 grouped into three layers with perpendicular and parallel components shown separately. In order to save space, plots show only halves of the waveforms for the parallel and for one of the perpendicular components. Similar decomposition for the magnetic field is shown in Fig. 3.

Noticeable in these plots is the electrostatic character of waves in panel 2a and electromagnetic character of waves in panels 2c, 3c. Also interesting is the large parallel electric field, as well as the compressional magnetic field present in all wave modes.

Frequency range between f_{cp} and f_{ce} is occupied by whistler and lower-hybrid waves which belong to the same branch of the dispersion equation but differ by the propagation direction and polarisation properties. LH waves propagate close to perpendicular direction and are mostly electrostatic, while whistlers have k-vectors in a wide angular range and become purely electromagnetic in the parallel direction. These two wave types can change their mode by conversion on the density gradients and striations (Rosenberg & Gekelman 2001; Eliasson & Papadopoulos 2008; Camporeale et al. 2012) that exist at the bow shock.

The analysis of the propagation direction for individual frequency dyads in the range 2–16 Hz shows that they propagate 120–140 degrees to the magnetic field, which implies that these are oblique whistler modes. The propagation direction is established both from the Poynting vector direction and the minimum variance of the wave magnetic field.

At 32 Hz and above, the propagation direction becomes perpendicular, the magnetic component diminishes rapidly

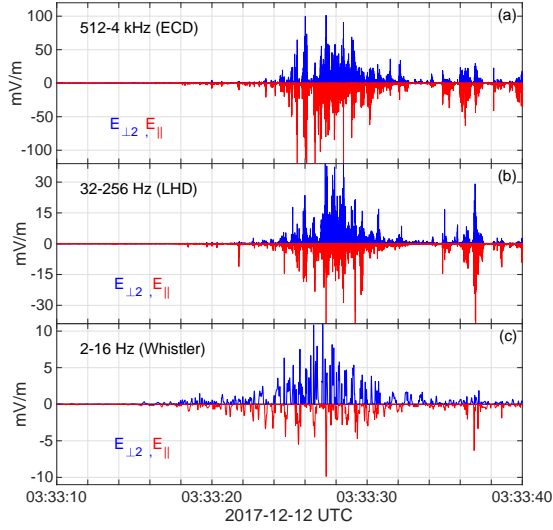


Figure 2. The measured electric vector, sampled at 8192 s^{-1} is decomposed into 3 bands using orthogonal wavelets (complete signal is exact sum of the components) and transformed to magnetic field-aligned coordinates (FAC). From the bottom: (c) obliquely propagating whistler waves (2–16 Hz), (b) Lower-Hybrid-Drift waves (32–256 Hz), and (a) Electron-Cyclotron-Drift waves (512–4000 Hz). To enhance readability we show only halves of the waveforms for the parallel and for one of the perpendicular components.

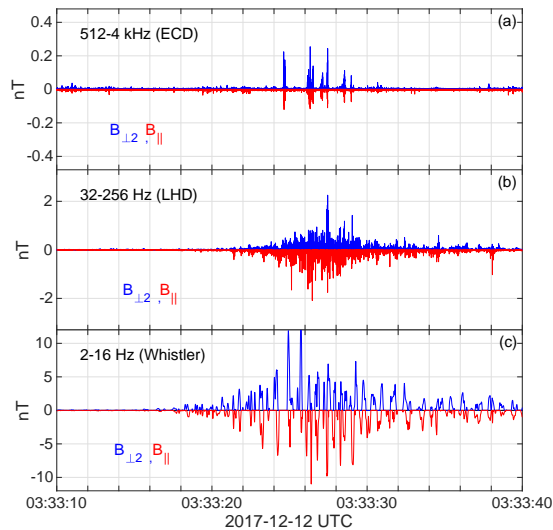


Figure 3. The measured magnetic signal is decomposed into 3 bands and shown in FAC coordinates as in Fig. 2.

with increasing frequency, indicating electrostatic, lower-hybrid character. These waves are most likely related to the LHD instability, which is a cross-field current-driven instability that couples LH waves with drift waves generated on the density gradients (Kral & Liewer 1971; Davidson et al. 1977; Daughton 2003). According to theory, there could be two types of instability. A weaker one – kinetic, should grow when the scale of the density gradient $L_n = (N^{-1}|\nabla N|)^{-1}$ is in

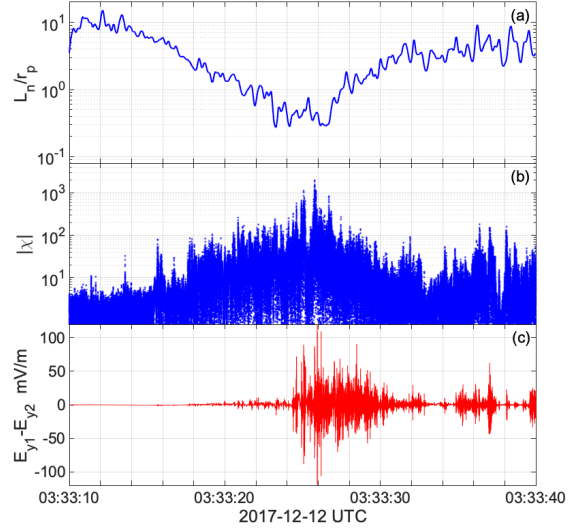


Figure 4. (a) Computed gradient scale of the density L_n normalised with proton gyroradius r_p showing that the region is strongly unstable for Lower-Hybrid-Drift waves ($L_n/r_p < 1$). (b) Timeseries of $|\chi|$, which correlates well with heating of ions and electrons. It contains 245,760 data points. (c) Difference $E_{y1} - E_{y2}$ of the electric field measured by satellites 1 and 2, separated by $\Delta y = 5 \text{ km}$.

the range $1 < L_n/r_p < (m_p/m_e)^{1/4}$, while the stronger, fluid-type instability occurs when $L_n/r_p < 1$. Here, r_p is a proton thermal gyroradius. The instability is caused by the diamagnetic ion drift $V_d = T_p(m_p\omega_{cp}L_n)^{-1} = v_{tp}(r_p/L_n)$. The maximum growth rate is at $k_{\perp}r_e \sim 1$, i.e. at wavelengths of a few electron gyroradii. These wavelengths will be Doppler shifted by the prevailing plasma flows $V \approx 300 \text{ km/s}$ to frequencies $f = V/(2\pi\lambda) \sim 40\text{--}70 \text{ Hz}$, in our case.

The scale L_n of the density gradient at the bow shock that can be determined directly by the MMS is indeed smaller than the ion gyroradius, as seen in Fig. 4a. This provides additional support for the interpretation that the bursty waves in the range $f_{lh} - f_{ce}$ of Figures 1 and 2b are mostly LHD waves. They are probably a permanent feature of quasi-perpendicular bow shocks because of the density ramp that drives the instability. Such waves have been observed also in other regions of the magnetosphere (Bale et al. 2002; Vaivads et al. 2004; Norgren et al. 2012; Graham et al. 2017).

Panel 2a contains electrostatic waves, which have been classified by first observers (Rodriguez & Gurnett 1975; Fuselier & Gurnett 1984) as ion-acoustic modes because of the large parallel electric field component. Waves in this frequency range have been analyzed with use of high-time resolution measurements obtained by THEMIS (Mozer & Sundqvist 2013; Wilson III et al. 2014), and by STEREO and Wind (Breneman et al. 2013), who noted large parallel electric fields and identified electron cyclotron harmonics in the spectra. Their conclusion that these are ECD waves is supported by the spectrum in Fig. 5 which shows seven f_{ce} harmonics.

The ECD instability (Forslund et al. 1972) is caused by the perpendicular relative ion-electron drift V_d comparable to the thermal electron speed v_{te} . It occurs at the resonance

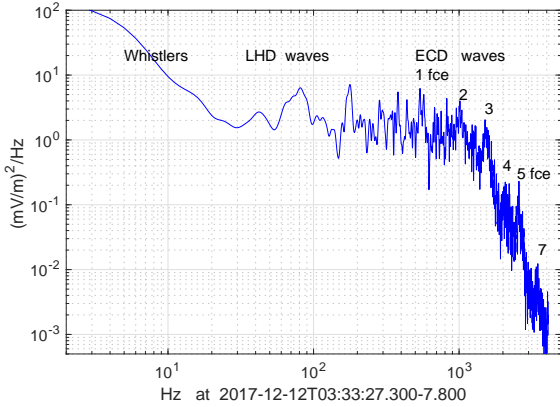


Figure 5. Power spectrum of E_{\perp} from the electron heating region. Obliquely propagating whistlers extend from 2 up to $f_{lh} \sim 16$ Hz followed by LHD waves. Clearly seen are Electron-Cyclotron-Drift waves with 7 harmonics starting from $f_{ce} \approx 500$ Hz.

$k(V_d - v_{tp}) = n\omega_{ce}$, couples electron Bernstein modes with ion-acoustic waves, and produces wavelengths smaller than the electron gyroradius (Lashmore-Davies 1971). In the current theoretical scenario (Muschiatti & Lembège 2013) this instability is presumably produced by ion beams reflected from the shock and moving perpendicularly against the solar wind and stationary electrons. This is a rather unrealistic scenario because two ion populations cannot have perpendicular ExB drift in opposite directions at the same time, and different from electrons (there are no other drifts in their model). This model would put the location of ion-beam driven ECD instability in front of the shock, around time 03:33:15 in our data, while the maximum of ECD waves is at 03:33:27 in the electron heating region. Despite the unrealistic scenario, the mathematics and conclusions of this paper are correct and valuable.

The data presented here suggest another mechanism for the ECD instability. The LHD electric fields of 20 mV/m in $B \sim 15$ nT produce ExB drift of 1300 km/s, comparable to the electron thermal speed. Since this field exists in narrow channels with a width of a few electron gyro-radii, only electrons can participate, making ion-electron drift $V_d \sim v_{te}$. Incidentally, this instability attracted attention of researchers working with Hall ion thrusters, because it affects their performance (Ducrocq et al. 2006; Boeuf & Garrigues 2018). In these devices, the instability is also caused by the ExB drift of electrons only, because ions have gyroradius larger than the drift channels.

The theory of ECD instability that links electron cyclotron harmonics with ion-acoustic waves and wavelengths at scales below the electron gyroradius provides convincing explanation for waves in panel 2a, which exhibit both large E_{\parallel} and E_{\perp} , contain f_{ce} harmonics, and Doppler shifted structures smaller than electron gyroradius.

3 WHAT HEATS IONS AND ELECTRONS?

We focus now on the fundamental question what kind of processes can increase the ion energy by 400 eV (from 50 to 450), and the electron energy by 50 eV (from 20 to 70 eV), within a few seconds, or during one proton gyro-period,

as seen in Fig. 1. Additional constraint is that heating of electrons is isotropic, while ions is mostly perpendicular.

The mechanism of stochastic ion heating on LH waves related to condition (1) has been explained by Karney (1979), and on other wave structures by other authors: Cole (1976); McChesney et al. (1987); Balikhin et al. (1993); Mishin & Banaszekiewicz (1998); Stasiewicz et al. (2000); Stasiewicz (2007); Vranjes & Poedts (2010); Stasiewicz et al. (2013); Yoon & Bellan (2019). The essence is that particles stressed by strong gradients (or equivalently by local space charges, $\text{div}(\mathbf{E}) = \rho/\epsilon_0$) lose adiabaticity and can be scattered along the electric field for direct acceleration by both DC- and wave-fields. The computed χ (Fig. 4b) shows values greatly exceeding 1, needed to stochastically perturb proton orbits, however, significant ion heating is observed when $\chi > 10$.

Formally, the error of χ is equivalent to the error of the electric field measurements, i.e., ~ 1 mV/m, or 10% of large amplitude fields, because of gain uncertainty in amplifiers (Lindqvist et al. 2016). However, in the case of ECD waves with wavelengths of the electron gyroradius, the gradient computations underestimate real values because the spacecraft separations are larger than wavelengths. In Figure 4c we show the difference in E_y components measured by satellites 1 and 2. Similar differences are seen on any pair of the satellites. A difference $\Delta E_y \approx 100$ mV/m on scales of the electron gyroradius $r_e \approx 1$ km in the field $B = 15$ nT would produce $\chi \approx 4600$, which could effectively demagnetise electrons and subject them to stochastic heating. Applying 10% error to this value would still maintain χ well above the required threshold for electron heating, which is reached in computations shown in Fig. 4b.

The presented data imply the following scenario for the rapid ion heating seen in Fig. 1. The diamagnetic current related to increasing density gradient at the foot of the shock (Fig. 4a) drives LH waves that couple/convert to oblique whistlers on density gradients and turn into LHD instability when the threshold is exceeded ($V_d \sim v_{tp}$). This results in increase of the wave amplitude, and cascade to shorter scales ($kr_e \sim 1$), which implies $\chi > 10$ that can perturb incoming solar wind ions. The ion energisation is probably a one step process (Stasiewicz 2007) (see Fig. 1 in that paper) in which ions gain energy from the DC electric field and not from wave fields. There is a quasi-DC (below 1 Hz) electric field of $E_0 = 5$ mV/m in this region. Protons stochastically perturbed by $\chi \sim 10-100$ on LHD waves (Fig. 4b), can be scattered along \mathbf{E}_0 , and acquire large perpendicular velocity during one gyro-period. To acquire 400 eV required for ion heating one needs electric potential from $E_0 = 5$ mV/m on a distance of 80 km. A displacement of ion gyrocenters by less than a gyroradius is sufficient to account for ion energisation.

Electrons require χ larger by a factor m_p/m_e to start stochastic heating. Apparently, amplitudes of LHD waves cannot produce gradients strong enough to make $\chi > 1836$ in the ion heating region of Fig. 1. However, as mentioned earlier, the electric field of LHD waves at ~ 20 mV/m can produce ExB drift of electrons comparable to the thermal velocity ($V_d = V_E \sim v_{te}$), which is needed to start ECD instability. This instability will produce stronger fields ~ 150 mV (Fig. 2a) and cascade to scales less than electron gyroradius, which would make $\chi > 1836$ and initiate electron heating. The mechanism for the ECD instability at the bow

shock is similar to that occurring in Hall thrusters. In both cases only electrons are drifting, because ions are prevented from the ExB drift by large gyroradius compared to the size of drift channels.

Stochastic heating of electrons occurs in localised bursts and is quenched by increasing B , because of the dependence $V_E \propto B^{-1}$ for the instability driver, and $\chi \propto B^{-2}$ for the stochastic condition. In most of the region, $\chi < m_p/m_e$, so the electrons respond adiabatically, $T_{e\perp} \propto B$, and a major part of the energy increase for electrons can be attributed to the increasing B at the ramp of the shock. Such perpendicular adiabatic heating must be accompanied by isotropization, possibly by E_{\parallel} of waves shown in Figure 2a.

It is interesting to note that by expressing $\text{div}(\mathbf{E}) \sim E/L_E$, and $V_E = E/B$ we can rewrite the condition $\chi_e > 1$ as

$$\frac{V_E}{v_{te}} > \frac{L_E}{r_e} \quad (2)$$

which implies that to start electron heating we need the ratio of the drift to thermal velocity exceeding the ratio of the electric gradient scale to the gyroradius. This fits properties of ECD waves, and the instability condition.

Another implication of equation (1) is the connection to charge non-neutrality. With typical $V_A \sim 100$ km/s at the bow shock, we need local charge non-neutrality exceeding 10^{-7} to start ion heating, and 2×10^{-4} to heat electrons. Also the presence of $E_{\parallel} \sim E_{\perp}$ in ECD waves in Fig. 2a is a natural consequence of space charges, which would produce electric fields in both directions.

4 CONCLUSIONS

The observations and the above analysis support the hypothesis on the universal character of the relation (1) and its applicability for identifying the heating processes of both electrons and ions, independent of the wave mode and the type of instability.

The plasma heating mechanism at quasi-perpendicular bow shocks appears to be a two-stage process. In the first stage, the *ion diamagnetic drift* on the density gradients, $V_d \sim v_{tp}$, ignites the LHD instability that produces $E \sim 20$ mV/m, and $\chi \gg 1$ that heats ions. In the second stage, the electric field of LHD waves produces *electron ExB drift*, $V_E \sim v_{te}$, which ignites the ECD instability that produces stronger fields, $E \sim 100$ mV/m, and $\chi > m_p/m_e$, that heats electrons. Part of the electron energy increase can be attributed to adiabatic heating $T_{e\perp} \propto B$ with isotropization by ECD waves.

The mechanism of the ECD instability at the bow shock is similar to the experimentally verified ECD instability in ion Hall thrusters, i.e., the ExB electron drift. All elements of the heating scenario described above have experimental support in MMS measurements.

Finally, it should be emphasised that this paper presents for the first time spectrum of the divergence of the electric field measured in space. Figure 1 is a time-frequency spectrogram of the electric charge distribution, weighted with B^{-2} , inside the bow shock. Obviously, it is an approximation, because gradients on small scales are not well resolved. The credits should go entirely to the members of the FIELDS consortium of the MMS project (Torbert et al.

2016; Lindqvist et al. 2016; Ergun et al. 2016) for designing the instruments and performing the project.

ACKNOWLEDGEMENTS

Special thanks to members of the FIELDS consortium of the MMS mission for making instruments capable of measuring divergence of the electric field in space. The author is grateful to Yuri Khotyaintsev for his invaluable help with the software for data processing. The MMS data are available to public via <https://lasp.colorado.edu/mms/sdc/public/>

REFERENCES

- Bale S. D., Mozer F. S., Phan T., 2002, *Geophys. Res. Lett.*, 29, 33
- Balikhin M., Gedalin M., 1994, *Geophys. Res. Lett.*, 21, 841
- Balikhin M., Gedalin M., Petrukovich A., 1993, *Phys. Rev. Lett.*, 70, 1259
- Boeuf J. P., Garrigues L., 2018, *Phys. Plasmas*, 25, 061204
- Breneman A. W., Cattell C. A., Kersten K., et al., 2013, *J. Geophys. Res.*, 118, 7654
- Burch J. L., Moore R. E., Torbert R. B., Giles B. L., 2016, *Space Sci. Rev.*, 199, 1
- Burgess D., Möbius E., Scholer M., 2012, *Space Sci. Rev.*, 173, 5
- Camporeale E., Delzanno G. L., Colestock P., 2012, *J. Geophys. Res.*, 117, A10315
- Cohen I. J., Schwartz S. J., Goodrich K. A., Ahmadi N., Ergun R. E., Fuselier S. A., et al., 2019, *J. Geophys. Res.*, 124, 3961
- Cole K. D., 1976, *Planet. Space Sci.*, 24, 515
- Daughton W., 2003, *Phys. Plasmas*, 10, 3103
- Davidson R. C., Gladd N. T., Wu C., Huba J. D., 1977, *J. Geophys. Res.*, 20, 301
- Ducrocq A., Adam J. C., Héron A., Laval G., 2006, *Phys. of Plasmas*, 13, 102111
- Eliasson B., Papadopoulos K., 2008, *J. Geophys. Res.*, 113, A09315
- Ergun R. E., et al., 2016, *Space Sci. Rev.*, 199, 167
- Escoubet C. P., Schmidt R., Russell C. T., 1997, *Space Sci. Rev.*, 79
- Forslund D., Morse R., Nielson C., Fu J., 1972, *Phys. Fluids*, 15, 1303
- Fuselier S. A., Gurnett D. A., 1984, *J. Geophys. Res.*, 89, 91
- Gary S. P., 1993, *Theory of space plasma microinstabilities*. Cambridge University Press
- Graham D. B., Khotyaintsev Y. V., Norgren C., et al., 2017, *J. Geophys. Res.*, 122, 517
- Harvey C. C., 1998, in Paschmann G., Daly P. W., eds, , Vol. SR-001 ISSI Reports, Analysis Methods for Multi-spacecraft Data. ESA, Chapt. 12, pp 307–322
- Karney C. F. F., 1979, *Phys. Fluids*, 22, 2188
- Krall N. A., Liever P. C., 1971, *Phys. Rev. A*, 4, 2094
- Lashmore-Davies C. N., 1971, *Phys. Fluids*, 14, 1481
- Le Contel O., et al., 2016, *Space Sci. Rev.*, 199, 257
- Lefebvre B., Schwartz S. J., Fazakerley A. F., Decreau P., 2007, *J. Geophys. Res.*, 112, A09212
- Lembège B., Savoini P., Balikhin M., Walker S., Krasnoselskikh V., 2003, *J. Geophys. Res.*, 108, 1256
- Lindqvist P.-A., Olsson G., Torbert R. B., King B., Granoff M., Rau D., Needell G., et al., 2016, *Space Sci. Rev.*, 199, 137
- Mallat S., 1999, *A wavelet tour of signal processing*. Academic Press
- McChesney J. M., Stern R., Bellan P. M., 1987, *Phys. Rev. Lett.*, 59, 1436
- Mishin E., Banaszekiewicz M., 1998, *Geophys. Res. Lett.*, 25, 4309

- Mozer F. S., Sundqvist D., 2013, *J. Geophys. Res.*, 118, 5415
- Muschietti L., Lembège B., 2013, *J. Geophys. Res.*, 118, 2267
- Ness N. F., Searce C. S., Seek H. B., 1964, *J. Geophys. Res.*, 69, 3531
- Norgren C., Vaivads A., Khotyaintsev Y., Andre M., 2012, *Phys. Rev. Lett.*, 109, 055001
- Pollock C., et al., 2016, *Space Sci. Rev.*, 199, 331
- Rodriguez P., Gurnett D., 1975, *J. Geophys. Res.*, 80, 19
- Rosenberg S., Gekelman W., 2001, *J. Geophys. Res.*, 106, 28,867
- Russell C. T., Anderson B. J., Baumjohann W., Bromund K. R., Dearborn D., Fischer D., Le G., et al., 2016, *Space Sci. Rev.*, 199, 189
- Sibeck D. G., Angelopoulos V., 2008, *Space Sci. Rev.*, 141, 35
- Stasiewicz K., 2007, *Plasma Physics and Controlled Fusion*, 49, B621
- Stasiewicz K., Lundin R., Marklund G., 2000, *Physica Scripta*, T84, 60
- Stasiewicz K., Markidis S., Eliasson B., Strumik M., Yamauchi M., 2013, *Europhys. Lett.*, 102, 49001
- Torbert R. B., et al., 2016, *Space Sci. Rev.*, 199, 105
- Treumann R. A., 2009, *Astron. Astrophys. Rev.*, 17, 409
- Vaivads A., André M., Buchert S. C., Wahlund J.-E., Fazakerly A. N., Cornilleau-Wehrin N., 2004, *Geophys. Res. Lett.*, 31
- Vranjes J., Poedts S., 2010, *MNRAS*, 408, 1835
- Wilson III L. B., Sibeck D. G., Breneman A. W., et al., 2014, *J. Geophys. Res.*, 119, 6475
- Wu C. S., et al., 1984, *Space Sci. Rev.*, 37, 63
- Yoon Y. D., Bellan P. M., 2019, *ApJL*, 887, L29

This paper has been typeset from a $\text{\TeX}/\text{\LaTeX}$ file prepared by the author.